ISSN 1066-3622, Radiochemistry, 2015, Vol. 57, No. 2, pp. 187–199 © Pleiades Publishing, Inc., 2015.
Original Russian Text © S.V. Yudintsev, S.V. Stefanovsky, B.S. Nikonov, M.S. Nikol'skii, T.S. Livshits, 2015, published in Radiokhimiya, 2015, Vol. 57, No. 2, pp. 161–171.

# Potential Matrices for Immobilization of the Rare Earth–Actinide Fraction of High-Level Waste in the $REE_2Zr_2O_7$–$REE_2Ti_2O_7$ System

**S. V. Yudintsev*[a], S. V. Stefanovsky[b], B. S. Nikonov[a], M. S. Nikol'skii[a], and T. S. Livshits[a]**

[a] *Institute of Geology of Ore Deposits, Petrography, Mineralogy, and Geochemistry, Russian Academy of Sciences, Staromonetnyi per. 35, Moscow, 119017 Russia*
[b] *Frumkin Institute of Physical Chemistry and Electrochemistry, Russian Academy of Sciences, Leninskii pr. 31, korp. 4, Moscow, 119071 Russia*
** e-mail: syud@igem.ru*

Received July 7, 2014

**Abstract**—Phase compositions, structural features, and element distributions were studied for samples of the compositions $REE_2(Zr_{2-x}Ti_x)O_7$, which are potential matrices for immobilization of the rare earth–actinide fraction of high-level waste from spent nuclear fuel reprocessing. Samples with $x$ up to 0.8 consist of pyrochlore, and at higher titanium content, of pyrochlore and monoclinic REE titanate with perovskite-type structure. The monoclinic phase becomes prevalent at $x > 1.2$. With respect to the content of the incorporated waste, it surpasses pyrochlore matrices by 10 wt %. The radiation resistance of this phase is close to that of titanate pyrochlore, but its amorphization dose is lower than for zirconate and titanate–zirconate pyrochlore. To check the suitability of monoclinic titanate for immobilization of the REE–actinide waste fraction, it is necessary to study its behavior in solutions and the effect of amorphization on the actinide leaching. The matrix can be prepared by the cold pressing–sintering method suggested in the United States for the synthesis of pyrochlore matrices with plutonium. High rate of solid-phase reactions in titanate systems allows the equilibrium to be attained at a moderate temperature (1400°C) within short sintering time (the first hours). One more possible procedure for matrix fabrication is cold crucible induction melting followed by the melt crystallization.

*Keywords: radioactive waste immobilization, rare earth–actinide fraction, pyrochlore matrices*

**DOI:** 10.1134/S1066362215020125

The progress of nuclear power engineering depends on the development of efficient methods for management of high-level waste (HLW) from spent nuclear fuel (SNF) reprocessing. Incorporation of HLW into special materials (matrices) for the disposal in an underground repository is the method that is the closest to practical implementation. Borosilicate and aluminophosphate glasses are used today for this purpose. Their drawbacks are well known [1]. These are low capacity for the waste, increase in the solubility in water with temperature, glass devitrification on heating due to radionuclide decay with worsening of the matrix properties, formation of highly mobile colloids on contact with water, etc. Glassy matrices are incapable of reliable isolation of long-lived radionuclides, including the most toxic actinides, for the time period of their potential hazard.

The waste management can be optimized by separation of groups (fractions) of radionuclides with different half-lives from HLW and their incorporation into different materials. Crystalline phases as matrices for actinides are advantageous over glasses owing to their higher resistance to corrosion and heat and higher HLW content that can be reached. Promising materials consist of phases of pyrochlore, zirconolite, murataite, britolite, and garnet structures (see [1–11] and other papers). A titanate ceramic was suggested in the United States for immobilization of excess weapons plutonium [11–14]. This ceramic consists to 80% of pyrochlore $(Ca,Gd,Pu,U)_2(Hf,Ti)_2O_7$, with the remainder constituted by brannerite $(U,Pu)Ti_2O_6$, zirconolite $(Ca,Gd)(Hf,U,Pu)(Ti,Al)_2O_7$, and rutile $(Ti,Hf)O_2$. The $PuO_2$ content of this matrix is 10–12 wt %; neutron absorbers (Hf, Gd, U) are introduced into the matrix to

**Table 1.** Content (g $t^{-1}$) of Am, Cm, and REE in SNF of different burn-up after 5-year storage and relative content of Am and Cm in the mixture (fraction) of trivalent actinides and REE [9, 21–25]

| Element | Burn-up, GW day $t^{-1}$ | | | | | | | |
|---|---|---|---|---|---|---|---|---|
| | 0.5 | 20 | 33 | 40 | 51 | 60 | 70 | 102 |
| ∑Am | 0.5 | 130 | 370 | 475 | 638 | 785 | 1080 | 1800 |
| ∑Cm | N/d[a] | N/d | 20 | N/d | 78 | 135 | N/d | 1370 |
| ∑REE | 220 | 7200 | 11 200 | ~15 000 | N/d | ~20 000 | ~23 000 | ~28 000 |
| (Am + Cm)/∑REE, % | 0.2[b] | 1.8[b] | 3.4 | 3.1[b] | N/d | 4.4 | 4.5[b] | 10.2 |

[a] (N/d) No data; [b] without curium.

avoid the chain fission reaction. A cold pressing–sintering method was suggested for fabricating this matrix; it has been implemented in glove boxes with the productive capacity of approximately 50 t annually. Commercial implementation would allow the whole amount of excess plutonium in the United States to be immobilized in 10 years. The scientific and demonstration parts of the program were fulfilled, but the practical implementation was not started because of the decision made in the early 2000s to abandon disposal of weapons plutonium and, instead, to utilize it in reactors in the form of mixed U–Pu oxide fuel [15].

Improvement of procedures for SNF reprocessing by extraction from aqueous solutions gave rise to new types of waste, in particular, to the rare earth–actinide HLW fraction. As a result, interest in crystalline matrices increased again. Because of complex composition of such waste, finding suitable matrices is more difficult than in the case of immobilization of Pu only. Nevertheless, the results obtained for Pu should be taken into account in the development of ceramics for immobilization of the rare earth–actinide HLW fraction. In this paper we characterize the properties of such potential matrices formed in the $REE_2Zr_2O_7$–$REE_2Ti_2O_7$ system.

**Table 2.** Variation with the storage time of the Am and Cm amounts (g $t^{-1}$ SNF) in the fuel with a burn-up of 45 GW day $t^{-1}$ and of their fractions in a mixture of REE and actinides [25]

| Radionuclide | 1 year | 5 years | 30 years |
|---|---|---|---|
| $^{241}$Am | 135 | 407 | 1272 |
| $^{243}$Am | 105 | 105 | 105 |
| ∑Am | 240 | 512 | 1377 |
| $^{242}$Cm | 3.8 | 0.1 | <0.01 |
| $^{244}$Cm | 35.3 | 30.3 | 11.6 |
| $^{245}$Cm | 2.2 | 2.2 | 2.2 |
| ∑Cm | 41.9[a] | 33.0[a] | 14.4[a] |
| Cm/(Am+Cm), % | 14.9 | 6.1 | 1.0 |
| Am + Cm fraction, %[b] | 1.8 | 3.5 | 8.5 |

[a] Differs from the sum of $^{242}$Cm, $^{244}$Cm, and $^{245}$Cm because of the presence of other Cm isotopes.

[b] Relative to the total REE content.

## COMPOSITION AND AMOUNT OF RARE EARTH–ACTINIDE FRACTION OF HLW FROM SNF REPROCESSING

The improved procedures for SNF reprocessing by extraction from aqueous solutions (TRUEX, UREX, UNEX) allow separation of a common group (fraction) of trivalent rare-earth and transplutonium (Am, Cm) elements (see [16–21] and other papers). The content of REE and actinides in SNF and HLW depends on the fuel burn-up and time of its storage prior to reprocessing (Tables 1, 2). As the burn-up of the fuel in light water reactors (PWR, WWER) is increased from 33 to 102 GW day $t^{-1}$, the Am content increases from 370 to 1800, and the Cm content, from 20 to 1370 g $t^{-1}$ SNF. The REE content increases from 11 to 28 kg $t^{-1}$ SNF (Table 1), with the content of specific elements decreasing in the order Nd > Ce > La > Pr, Sm >> Y. With the SNF storage time, the content of short-lived nuclides $^{241}$Pu (half-life $T_{1/2}$ = 14 years) and $^{244}$Cm ($T_{1/2}$ = 18 years) decreases, and that of their daughter nuclides, $^{241}$Am (433 years) and $^{240}$Pu (6537 years), increases. The $^{237}$Np content also increases owing to the $^{241}$Am decay, etc. On the other hand, the major fraction of radioactive lanthanide isotopes ($^{144}$Ce, $^{152,154,155}$Eu, $T_{1/2}$ < 13 years) undergoes decay to stable daughter nuclides. After 5-year storage, 1 t of SNF with the burn-up of 60 GW day $t^{-1}$ contains 785 g of Am (including 63% $^{241}$Am, 37% $^{243}$Am), 135 g of Cm (90% $^{244}$Cm, 8% $^{245}$Cm, 1% $^{243}$Cm, 1% $^{246}$Cm), and approximately 20 kg of REE. At a typical burn-up of light water reactor fuel of 45 GW day $t^{-1}$, the amount of REE and trivalent actinides per ton of SNF after

5-year storage (by the reprocessing time) will be 13.9 and 0.87 kg, respectively [17].

All these factors will influence the ratio of elements in the rare earth–actinide HLW fraction. Its major components are cerium-group lanthanides, and the content of actinides (Am, Cm) and their decay products does not exceed 5 wt %. The relative content of actinides in the fraction will increase as the SNF burn-up and storage time prior to reprocessing are increased. Long-lived actinides initially present in SNF and produced by the decay of short-lived predecessors (Table 3) determine the SNF and HLW radiotoxicity for many thousands of years [1, 7, 9, 17]. If all the actinides are considered, only after 100000 years their toxicity will decrease to the level of natural uranium used for the fuel fabrication [1, 17]. As for the rare earth–actinide fraction, this will take place after 6000 years, with the main hazard associated with $^{241}$Am and $^{243}$Am and with their decay products ($^{237}$Np, $^{239}$Pu).

One light water reactor produces about 20 t of SNF annually. A plant for reprocessing 800 t of SNF annually generates 4000 m$^3$ of liquid HLW containing 90 g of Am and Cm in 1 m$^3$ of the waste [17]. The park of reactors with the total power of 100 GW (el.), e.g., in the United States or West Europe, produces up to 3.2 t of minor actinides annually [17]: 1.6 t of Np and 1.6 t of the sum of Am and Cm, and the total weight of the rare earth–actinide fraction in this HLW volume will be about 30 t.

**Table 3.** Transuranium actinides in spent uranium fuel

| Isotope | $T_{1/2}$, years | Decay type | Daughter isotope |
|---|---|---|---|
| $^{237}$Np | $2.14 \times 10^6$ | α | $^{233}$Pa |
| $^{238}$Pu | 87.7 | α | $^{234}$U |
| $^{239}$Pu | $2.41 \times 10^4$ | α | $^{235}$U |
| $^{240}$Pu | 6537 | α | $^{236}$U |
| $^{241}$Pu | 14.4 | $\beta^-$ | $^{241}$Am |
| $^{242}$Pu | $3.76 \times 10^5$ | α | $^{238}$U |
| $^{244}$Pu | $8 \times 10^7$ | α | $^{240}$U |
| $^{241}$Am | 433 | α | $^{237}$Np |
| $^{242m}$Am | 141 | IT | $^{242}$Am |
| $^{242}$Am | 16 h | $\beta^-$ ($^{242}$Cm), EC ($^{242}$Pu) | |
| $^{243}$Am[a] | $7.3 \times 10^3$ | α | $^{239}$Pu |
| $^{242}$Cm | 0.4 | α | $^{238}$Pu |
| $^{243}$Cm | 29.1 | α | $^{239}$Pu |
| $^{244}$Cm | 18.1 | α | $^{240}$Pu |
| $^{245}$Cm | $8.5 \times 10^3$ | α | $^{241}$Pu |
| $^{246}$Cm | $4.76 \times 10^3$ | α | $^{242}$Pu |

[a] First $^{239}$Np is produced ($T_{1/2}$ = 2.36 days), and then it transforms into $^{239}$Pu.

## POTENTIAL MATRICES FOR IMMOBILIZATION OF THE RARE EARTH–ACTINIDE FRACTION

Immobilization of the rare earth–actinide HLW fraction into ceramic matrices, followed by their disposal in underground tunnels, is the best procedure for management of such wastes. This approach allows efficient utilization of the underground space of the repositories and enhances the safety of the disposal of long-level HLW owing to the use of a stable matrix.

The titanates of the pyrochlore structure, suggested for immobilization of tetravalent actinides (Pu, Np), cannot be used as matrices for the rare earth–actinide fraction. This is caused by the fact that the pyrochlore structure of $Ln_2Ti_2O_7$ phases is characteristic only of compounds of heavy lanthanides (Ln) with the cation size smaller than that of $Pm^{3+}$ [11, 26, 27]. Titanates of light REE, prevalent in the rare earth–actinide fraction, have the monoclinic structure of the perovskite type, similar to that of $Pu_2Ti_2O_7$ and $Am_2Ti_2O_7$ [26]. Replacement of the $Ti^{4+}$ cation by the larger $Zr^{4+}$ and $Sn^{4+}$ cations stabilizes the pyrochlore lattice [2–4], but the phase formation in this case occurs slowly even at temperatures exceeding 1500°C [28, 29]. Therefore, residues of the initial charge remain in the synthesis products, which deteriorates the isolation properties of actinide waste matrices. Another method of stabilizing the pyrochlore structure of titanate phases is incorporation of elements with a small cation radius like Lu [27] or Y. Such dilution decreases the capacity of the matrix for the waste by approximately 20%.

Previous studies of titanates of the composition $Ln_2Ti_2O_7$ (Ln = La, Ce, Nd) with the structure of perovskite type mainly concerned their dielectric properties [30–34]. In several studies, these materials were studied as matrices for trivalent actinides [27, 35–41]. These studies were aimed at determining the fields of the perovskite-type phases in the $Nd_2O_3$–$ZrO_2$–$TiO_2$ and $Nd_2O_3$–$TiO_2$ systems, their behavior in the course of ionic irradiation, and the stability in solution. Of particular interest are the results obtained for the neodymium-containing ceramics, as the ionic radius of $Nd^{3+}$ (1.11 Å) is close to the mean ionic radius of the elements of the rare-earth–actinide fraction [3, 42]. In addition, Nd prevails in the rare earth–actinide fraction. To proceed with such studies further, we synthe-

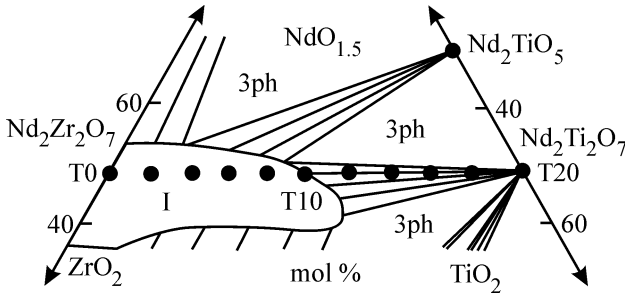


**Рис. 1.** Position of the sample compositions in the $NdO_{1.5}$–$ZrO_2$–$TiO_2$ phase diagram [35]. (I) Pyrochlore field; fields of two-phase associations are cross-hatched; (3ph) fields of coexistence of three phases.

sized and examined samples of the series $REE_2Zr_2O_7$–$REE_2Ti_2O_7$, where REE is the sum of elements taken in a ratio close to their relative content in the rare earth–actinide fraction.

## SYNTHESIS OF SAMPLES AND INVESTIGATION METHODS

The charge for the synthesis was prepared from the oxides $TiO_2$, $ZrO_2$, and $REE_2O_3$, taken in amounts corresponding to the formula $REE_2Zr_{2-x}Ti_xO_7$, with $x$ varied from 0 (sample T0) to 2 (T20) with a step of 0.1–0.2. The element proportions (wt %) in the REE mixture were as follows: $La_2O_3$ 11.8, $Ce_2O_3$ 23.0, $Pr_2O_3$ 10.7, $Nd_2O_3$ 38.9, $Sm_2O_3$ 8.1, $Eu_2O_3$ 1.3, $Gd_2O_3$ 1.5, and $Y_2O_3$ 4.7. The radii of the $Sm^{3+}$ and $Nd^{3+}$ cations are close to those of the $Am^{3+}$ and $Cm^{3+}$ cations; therefore, Sm and Nd were chosen for simulating the behavior of Am and Cm. Cerium existing in oxidation states (III, IV) simulated plutonium. The mixtures after the homogenization were pressed in pellets (200 atm, 25°C) and sintered for 5 h at 1400 (Zr : Ti ≤ 1) or 1550°C (Zr : Ti > 1). It is known that the phase formation in titanate systems with REE is complete at 1300–1400°C in 1–3 h [28]. At high Zr content, elevated temperature is required to accelerate the reactions. The structure of the examined part of the $NdO_{1.5}$–$ZrO_2$–$TiO_2$ system and the positions of the sample compositions are shown in Fig. 1.

Samples were studied with a Rigaku D/Max 2200 X-ray diffractometer (XRD, Cu$K_\alpha$) and with a JSM-5610LV scanning electron microscope equipped with a JED-2300 energy-dispersive X-ray spectrometer (SEM/EDX). For samples T4 and T18, X-ray absorption fine structure (XAFS) spectra were recorded at the Kurchatov institute with the radiation source in the transmission geometry. To evaluate the radiation resistance, samples T0, T18, and T20 were irradiated in the temperature interval 50–950 K at the accelerator of the Argonne National Laboratory (the United States) with 1-MeV $Kr^{2+}$ ions at a flux density of $10^{11}$–$10^{12}$ ions $cm^{-2}$ $s^{-1}$.

## RESULTS OF X-RAY DIFFRACTION ANALYSIS

The X-ray diffraction patterns of samples T0–T8 ($x$ = 0–0.8) are relatively simple (Fig. 2). They contain four strong reflections and a series of weak (satellite) reflections allowing the phase structure to be identified as a cubic structure of pyrochlore type (space group $Fd3m$, $Z$ = 8). These weak reflections with odd indices ($hkl$) distinguish the X-ray diffraction pattern of phases of pyrochlore structure from those of compounds with the fluorite-type lattice. The interplanar spacing $d_{222}$ of pyrochlore decreases from 3.050 Å in sample T0 to 2.969 Å in T18 because of a decrease in its unit cell size from 10.57 to 10.28 Å with variation of the composition (replacement of $Zr^{4+}$ by the smaller $Ti^{4+}$ cation).

Three weak reflections ($d$ = 4.141, 3.200, 2.944 Å) of a second phase appear for the first time in the X-ray diffraction pattern of sample T8. As the titanium content is increased, these reflections grow in intensity, numerous additional peaks appear, and the diffraction pattern becomes more complex (Fig. 2). The set of the newly appearing reflections corresponds to monoclinic titanate with perovskite-type structure (space group $P2_1$, $Z$ = 8) of the formula $Nd_2Ti_2O_7$ (compound 33-0942 in JCPDS database [43]).

## RESULTS OF SEM/EDX STUDY

According to the data of scanning electron microscopy (Fig. 2, Tables 4–6), samples T0–T6 consist only of pyrochlore forming grains of size smaller than 10 μm. Its composition is close to the calculated composition. An unexpected result is high Y content of pyrochlore in sample T8 relative to the calculated value. This may be associated with errors in preparation of the starting charge for synthesis of this ceramic. In sample T8, there are very fine dark inclusions in the bulk of pyrochlore (Fig. 2). Specifically these inclusions are, probably, the monoclinic phase whose weak reflections are seen in the X-ray diffraction pattern. However, because of small size of these inclusions (fractions of micrometer, which is smaller than the

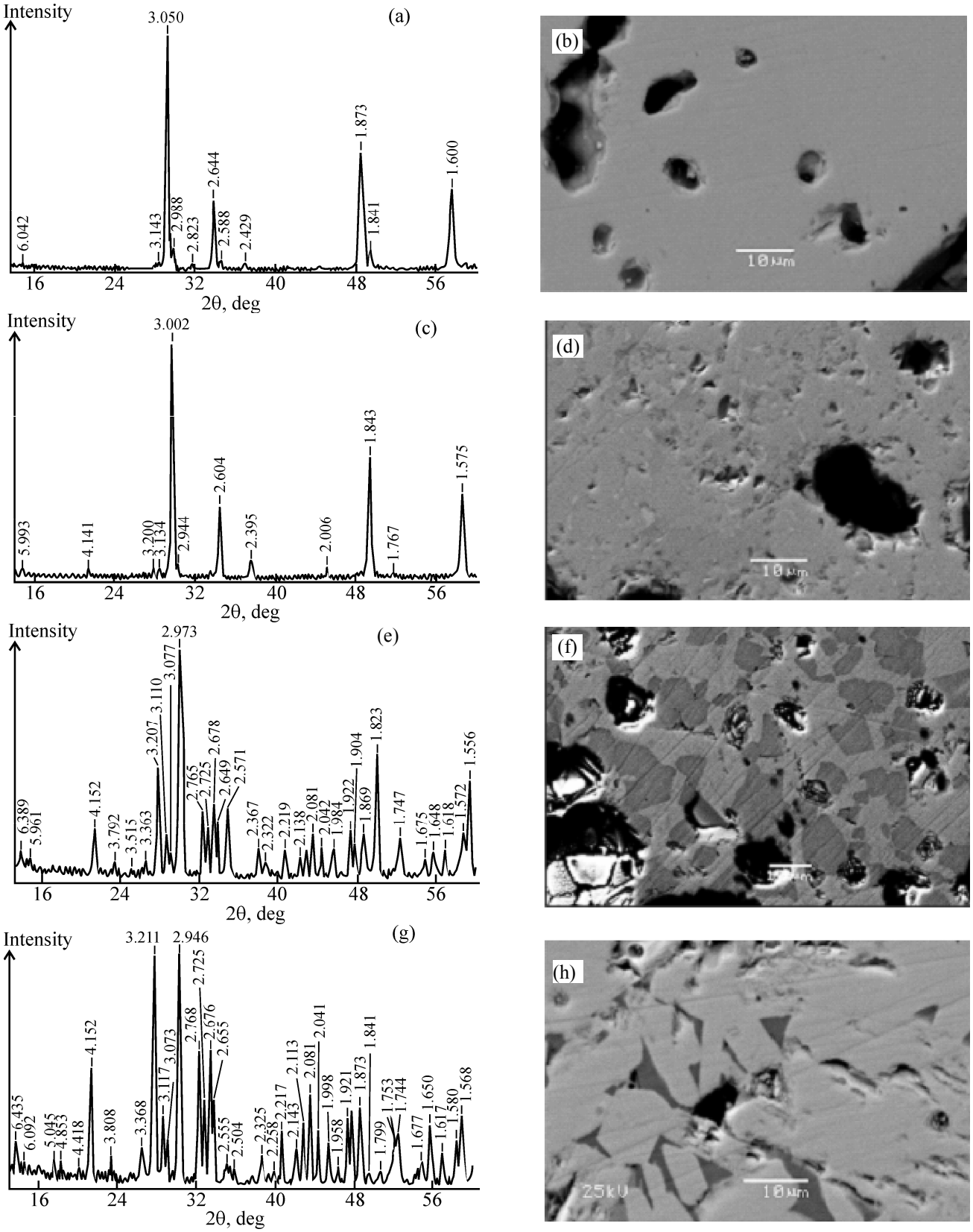


**Fig. 2.** (a, c, e, g) X-ray diffraction patterns and (b, d, f, h) SEM/EDX images of samples (a, b) T0, (c, d) T8, (e, f) T16, and (g, h) T20. Numerals in the X-ray diffraction patterns are interplanar spacings, Å. Gray areas: (b, d) pyrochlore or (f, h) titanate of perovskite structure; dark areas: (d) titanate of perovskite structure or (f, h) pyrochlore; black areas: pores. Scale bar: 10 μm.

**Table 4.** Composition of pyrochlore in samples T0–T8 (SEM/EDX data, ∑ = 100%)[a]

| Oxide, ion | T0 | T2 | T4 | T6 | T8 |
|---|---|---|---|---|---|
| $TiO_2$ | None | 5.0 | 7.4 | 9.4 | 13.1 |
| $ZrO_2$ | 45.7 | 39.7 | 34.3 | 35.2 | 29.5 |
| $Y_2O_3$ | 2.6 | 2.1 | 2.3 | 2.3 | 7.5 |
| $La_2O_3$ | 7.5 | 7.9 | 6.0 | 7.4 | 7.3 |
| $Ce_2O_3$ | 12.6 | 12.2 | 12.5 | 14.0 | 12.8 |
| $Pr_2O_3$ | 5.1 | 5.5 | 5.2 | 6.1 | 4.8 |
| $Nd_2O_3$ | 19.2 | 21.2 | 18.6 | 19.6 | 19.4 |
| $Sm_2O_3$ | 3.7 | 4.0 | 9.5 | 3.5 | 3.2 |
| $Eu_2O_3$ | 1.7 | 0.9 | 2.4 | 1.1 | 0.9 |
| $Gd_2O_3$ | 1.9 | 1.5 | 1.8 | 1.4 | 1.5 |
| $Ti^{4+}$ | None | 0.33 | 0.50 | 0.80 | 0.82 |
| $Zr^{4+}$ | 2.00 | 1.67 | 1.50 | 1.20 | 1.18 |
| $Y^{3+}$ | 0.12 | 0.10 | 0.11 | 0.10 | 0.33 |
| $La^{3+}$ | 0.25 | 0.25 | 0.20 | 0.23 | 0.22 |
| $Ce^{3+}$ | 0.41 | 0.38 | 0.41 | 0.42 | 0.39 |
| $Pr^{3+}$ | 0.17 | 0.17 | 0.17 | 0.18 | 0.15 |
| $Nd^{3+}$ | 0.62 | 0.65 | 0.59 | 0.58 | 0.57 |
| $Sm^{3+}$ | 0.11 | 0.12 | 0.29 | 0.10 | 0.09 |
| $Eu^{3+}$ | 0.05 | 0.03 | 0.07 | 0.03 | 0.02 |
| $Gd^{3+}$ | 0.06 | 0.04 | 0.06 | 0.04 | 0.04 |
| ∑cations | 3.79 | 3.75 | 3.90 | 3.68 | 3.82 |
| $O^{2-}$ | 6.69 | 6.62 | 6.86 | 6.53 | 6.72 |
| REE/(Zr + Ti) | 0.90 | 0.87 | 0.95 | 0.84 | 0.90 |

[a] The content of oxides is given in wt %, and the content of ions, in the form of stoichiometric coefficients in the formulas, counting on Zr + Ti = 2. The same in Tables 5 and 6.

**Table 5.** Compositions of the pyrochlore (p), monoclinic (m), and oxide (o) phases in samples T10–T14

| Oxide, ion | T10-p | T10-m | T12-p | T12-m | T12-o | T14-p | T14-m | T14-o |
|---|---|---|---|---|---|---|---|---|
| $TiO_2$ | 13.3 | 31.8 | 14.2 | 32.5 | 4.4 | 15.7 | 31.9 | 6.2 |
| $ZrO_2$ | 29.5 | 1.5 | 30.3 | 1.3 | 44.5 | 27.6 | 1.2 | 45.1 |
| $Y_2O_3$ | 5.2 | 1.3 | 3.3 | 1.1 | 2.7 | 3.9 | 1.7 | 3.7 |
| $La_2O_3$ | 7.6 | 20.9 | 4.4 | 14.6 | 1.8 | 5.0 | 13.9 | 2.8 |
| $Ce_2O_3$ | 12.3 | 11.6 | 13.8 | 15.8 | 26.0 | 13.9 | 13.6 | 22.0 |
| $Pr_2O_3$ | 5.6 | 7.0 | 4.9 | 6.7 | 2.3 | 5.5 | 6.7 | 2.5 |
| $Nd_2O_3$ | 18.3 | 20.0 | 20.7 | 22.2 | 11.5 | 20.4 | 23.7 | 11.0 |
| $Sm_2O_3$ | 5.2 | 3.9 | 4.5 | 3.1 | 3.2 | 4.8 | 3.9 | 3.7 |
| $Eu_2O_3$ | 1.4 | 1.2 | 1.2 | 1.1 | 1.3 | 1.7 | 2.1 | 1.4 |
| $Gd_2O_3$ | 1.6 | 0.8 | 2.8 | 1.7 | 2.3 | 1.5 | 1.1 | 1.6 |
| $Ti^{4+}$ | 0.82 | 1.95 | 0.83 | 1.95 | 0.27 | 0.94 | 1.95 | 0.34 |
| $Zr^{4+}$ | 1.18 | 0.05 | 1.17 | 0.05 | 1.73 | 1.06 | 0.05 | 1.66 |
| $Y^{3+}$ | 0.23 | 0.06 | 0.14 | 0.05 | 0.12 | 0.16 | 0.07 | 0.15 |
| $La^{3+}$ | 0.23 | 0.63 | 0.13 | 0.43 | 0.05 | 0.15 | 0.42 | 0.08 |
| $Ce^{3+}$ | 0.37 | 0.34 | 0.40 | 0.46 | 0.76 | 0.40 | 0.41 | 0.60 |
| $Pr^{3+}$ | 0.17 | 0.21 | 0.14 | 0.20 | 0.07 | 0.16 | 0.20 | 0.07 |
| $Nd^{3+}$ | 0.53 | 0.58 | 0.58 | 0.63 | 0.33 | 0.57 | 0.69 | 0.29 |
| $Sm^{3+}$ | 0.15 | 0.11 | 0.12 | 0.09 | 0.09 | 0.13 | 0.11 | 0.09 |
| $Eu^{3+}$ | 0.04 | 0.03 | 0.03 | 0.03 | 0.04 | 0.05 | 0.06 | 0.04 |
| $Gd^{3+}$ | 0.04 | 0.02 | 0.07 | 0.04 | 0.06 | 0.04 | 0.03 | 0.04 |
| ∑cations | 3.76 | 3.98 | 3.61 | 3.92 | 3.52 | 3.67 | 3.98 | 3.35 |
| $O^{2-}$ | 6.64 | 6.97 | 6.42 | 6.89 | 6.28 | 6.50 | 6.97 | 6.03 |
| REE/(Zr + Ti) | 0.88 | 0.99 | 0.80 | 0.97 | 0.76 | 0.83 | 0.99 | 0.68 |

**Table 6.** Compositions of the pyrochlore (p) and monoclinic (m) phases in samples T15–T20

| Oxide, ion | T15-p | T15-m | T16-p | T16-m | T18-p | T18-m | T20-p | T20-m |
|---|---|---|---|---|---|---|---|---|
| $TiO_2$ | 19.8 | 33.0 | 21.5 | 32.3 | 26.4 | 33.1 | 41.6 | 33.4 |
| $ZrO_2$ | 23.7 | 1.6 | 21.8 | 1.2 | 16.4 | 0.7 | None | None |
| $Y_2O_3$ | 5.8 | 2.4 | 4.9 | 1.8 | 6.8 | 2.2 | 8.0 | 2.9 |
| $La_2O_3$ | 4.2 | 11.6 | 3.9 | 11.2 | 3.5 | 10.4 | 3.4 | 8.9 |
| $Ce_2O_3$ | 12.6 | 16.2 | 12.9 | 16.9 | 11.8 | 17.0 | 15.0 | 16.0 |
| $Pr_2O_3$ | 5.1 | 6.5 | 4.7 | 6.5 | 4.8 | 6.4 | 2.7 | 6.0 |
| $Nd_2O_3$ | 20.3 | 23.3 | 21.9 | 24.8 | 21.0 | 23.6 | 21.0 | 25.1 |
| $Sm_2O_3$ | 5.4 | 3.8 | 4.6 | 3.3 | 5.4 | 4.2 | 3.6 | 5.2 |
| $Eu_2O_3$ | 1.2 | 0.7 | 1.5 | 0.9 | 1.6 | 1.1 | 2.7 | 1.4 |
| $Gd_2O_3$ | 1.9 | 0.9 | 2.1 | 1.1 | 2.4 | 1.3 | 2.0 | 1.2 |
| $Ti^{4+}$ | 1.21 | 1.94 | 1.21 | 1.96 | 1.43 | 1.97 | 2.00 | 2.00 |
| $Zr^{4+}$ | 0.79 | 0.06 | 0.79 | 0.05 | 0.57 | 0.03 | None | None |
| $Y^{3+}$ | 0.23 | 0.10 | 0.19 | 0.07 | 0.26 | 0.09 | 0.27 | 0.12 |
| $La^{3+}$ | 0.12 | 0.33 | 0.11 | 0.33 | 0.09 | 0.31 | 0.08 | 0.26 |
| $Ce^{3+}$ | 0.35 | 0.46 | 0.35 | 0.50 | 0.31 | 0.50 | 0.35 | 0.47 |
| $Pr^{3+}$ | 0.14 | 0.19 | 0.13 | 0.19 | 0.12 | 0.19 | 0.06 | 0.17 |
| $Nd^{3+}$ | 0.55 | 0.65 | 0.58 | 0.71 | 0.54 | 0.67 | 0.48 | 0.71 |
| $Sm^{3+}$ | 0.14 | 0.10 | 0.12 | 0.09 | 0.13 | 0.12 | 0.08 | 0.14 |
| $Eu^{3+}$ | 0.03 | 0.02 | 0.04 | 0.03 | 0.04 | 0.03 | 0.06 | 0.04 |
| $Gd^{3+}$ | 0.05 | 0.02 | 0.05 | 0.03 | 0.06 | 0.03 | 0.04 | 0.03 |
| ∑cations | 3.61 | 3.88 | 3.57 | 3.96 | 3.56 | 3.93 | 3.43 | 3.95 |
| $O^{2-}$ | 6.42 | 6.82 | 6.36 | 6.94 | 6.34 | 6.89 | 6.14 | 6.92 |
| REE/(Zr + Ti) | 0.80 | 0.94 | 0.78 | 0.98 | 0.77 | 0.97 | 0.71 | 0.97 |

area of SEM/EDX analysis), we could not determine the composition of these inclusions. In sample T10, the content of this phase is high, and it forms elongated dark grains in the bulk of the pyrochlore phase (light in the image). The grain size for all the phases is several times larger (up to 10–15 μm) compared to the samples with higher Zr content, consisting of pyrochlore only.

In sample T12, these phases are present in close amounts. The pyrochlore phase is enriched in Zr and Y, whereas the monoclinic phase is enriched in Ti and cerium-group REE, especially La, and the concentration of Zr in it is low. A specific feature of samples T10–T14 is appearance of a small amount (first percents) of one more phase in gaps between the grains of the two major phases. The third phase has light color in the images, and the size of its inclusions reaches several micrometers. The prevalent components of this phase are Zr, Ce, and Nd (Table 5), which allows this phase to be identified as a solid solution of oxides of these elements. The position of its grains between the crystals of the major phases (monoclinic and cubic) suggests its formation in the course of the sample synthesis, rather than preservation of relics of the starting charge.

As the $TiO_2$ content is increased, the amount of pyrochlore in the sample decreases, and the fraction of the monoclinic phase increases. In samples T15–T18, pyrochlore grains are already embedded in the bulk of the monoclinic phase (Fig. 2). The grain size changes to dark for pyrochlore and light for the monoclinic phase because of higher mean atomic mass of the latter phase. In sample T20, in which the monoclinic phase prevails, two more phases are present in small amounts. The first phase in accordance with its composition can be assigned to pyrochlore. As compared to the monoclinic phase, it has higher content of Ti and REE with small ionic radii (Y, Eu, Gd). In the monoclinic phase, the concentrations of La and Pr are three times higher, and those of Nd and Sm, 1.5 times higher than in pyrochlore (on the atomic scale). The Ce distribution seems unusual. If it were present exclusively in the trivalent state ($r$ = 1.14 Å), its behavior would be similar to that of $La^{3+}$ (1.16 Å) and $Pr^{3+}$ (1.13 Å), with

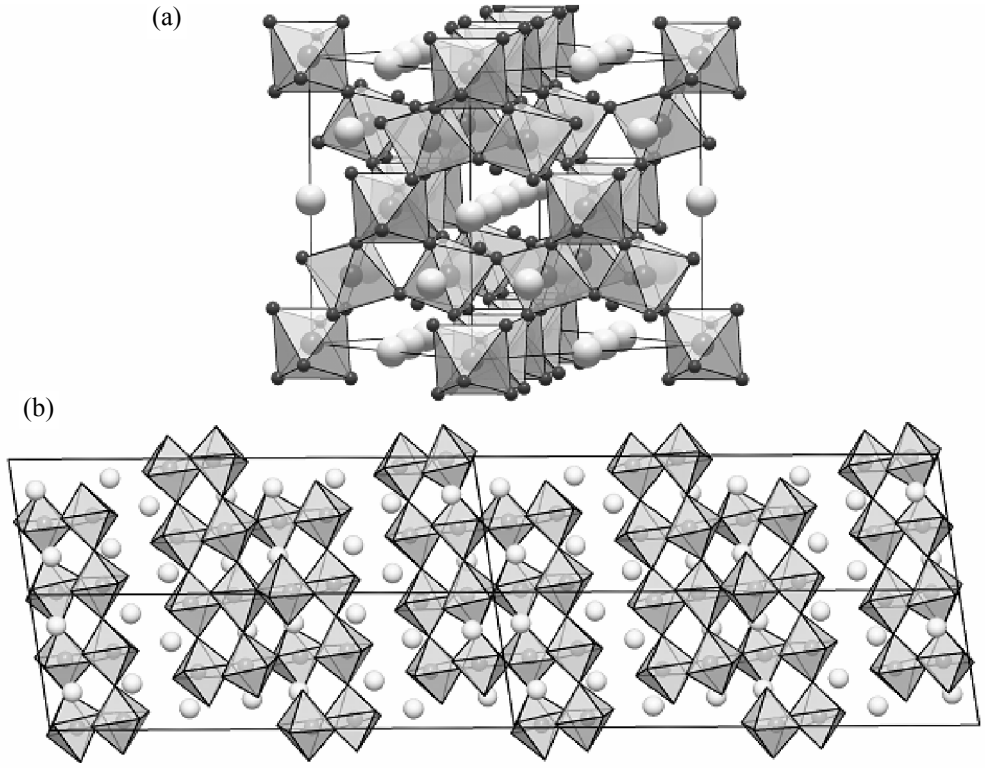


**Fig. 3.** Structure of (a) pyrochlore in the direction close to [101] and (b) titanate of perovskite structure in the [010] direction; cell size 2 × 2. Large circles: rare earth cations; (a) small circles: oxygen anions.

manifold enrichment of the monoclinic phase. However, actually the phases differ in the Ce content by only 30%. This may be attributed to possible presence of $Ce^{4+}$ (0.97 Å) in the sample along with $Ce^{3+}$, with the $Ce^{4+}/Ce^{3+}$ ratio in pyrochlore being higher than in the monoclinic phase. REE cations of small size stabilize the cubic structure; therefore, high content of Y and Ce (especially $Ce^{4+}$) allows this phase to be identified as pyrochlore.

The second impurity phase of sample T20 has the following composition, wt %: 51.7 $TiO_2$, 2.0 $Y_2O_3$, 8.1 $La_2O_3$, 15.0 $Ce_2O_3$, 3.8 $Pr_2O_3$, 16.9 $Nd_2O_3$, 0.4 $Sm_2O_3$, 1.0 $Eu_2O_3$, and 1.1 $Gd_2O_3$. It is arranged between the grains of the monoclinic phase and is characterized by darker color in the SEM images. The REE : Ti : O atomic ratio in it is 0.91 : 2 : 5.37, which is close to that in $Ln_4Ti_9O_{24}$ (0.89 : 2 : 5.33). In the titanium-rich part of the systems $Ln_2O_3$–$TiO_2$ (Ln = La, Ce, Nd), there is a compound of the composition $Ln_4Ti_9O_{24}$, crystallizing in the rhombic system [30–34]. The reflections of this compound in the X-ray diffraction pattern of sample T20 were not revealed because of its low content and/or overlap by the peaks of the prevalent monoclinic phase.

The pyrochlore phase is characterized by a wide range of composition variation, especially with respect to the $TiO_2$ and $ZrO_2$ content. In samples T0–T18, the $ZrO_2$ content of the pyrochlore phase decreases from 45.7 to 16.4 wt %, whereas the $TiO_2$ content increases from 0 to 33 wt % (Tables 4–6). The Zr content of the monoclinic phase does not exceed 2 wt %. Introduction of larger amounts of Zr into the charge (or their presence in HLW) leads to the formation of the pyrochlore phase with the Ti/Zr ratio close to unity 1. The content of the simulated rare earth–actinide fraction increases from 56 wt % for zirconate pyrochlore (sample T0) to 67 wt % for monoclinic titanate (sample T20).

## SPECIFIC FEATURES OF CRYSTAL CHEMISTRY OF PHASES IN THE $REE_2Zr_2O_7$–$REE_2Ti_2O_7$ SYSTEM

Variations of the compositions of the pyrochlore and monoclinic titanate phases are caused by their crystallochemical features. The pyrochlore structure is based on a framework of $BO_6$ octahedra sharing common vertices, with large REE and actinide cations located in the voids (Fig. 3). It arises from the related

fluorite-type structure on removing one anion from the junction of four cubes and replacing a half of cubes by octahedra. As a result, the phase stoichiometry transforms from $^{[8]}A_4X_8$ into $^{[8]}A_2{}^{[6]}B_2X_6Y$, where A and B are cations, and X and Y are anions. Some of them ($X = O^{2-}$) occupy the vertices of the $BO_6$ octahedron, and other anions ($Y = O^{2-}$, $F^-$, $OH^-$) are not incorporated in the framework and occupy a particular position in the structure. The pyrochlore unit cell size (9.3–12.0 Å) is approximately two times larger than that of oxides with the fluorite-type lattice. This structure can be presented in the form of networks of $B_2X_6$ octahedra and $A_2Y$ tetrahedra in which cations A and anions Y are arranged in channels and are weakly bound to the framework. The possibility of the formation of defective structures with vacancies in the A and Y positions is associated with this feature. For the pyrochlore lattice to be stable, the ratio of the radii of cations A and B ($r_A/r_B$) should be in the range from 1.46 to 1.80 [4, 11, 26]. At lower values of this ratio, cubic structure of the fluorite type is stable, and at higher values the monoclinic perovskite-like structure is stabilized. This condition is met for zirconates of cerium-group REE (up to Gd) and for titanates of middle and yttrium-group REE.

Monoclinic titanates of trivalent REE with large cation size (from La to Pm) of the formula $REE_2Ti_2O_7$ have the structure consisting of perovskite-type layers (Fig. 3) with a thickness of four $TiO_6$ octahedra, parallel to (110). The adjacent layers are shifted by a distance of a half of the $TiO_6$ octahedron and are separated from each other by a double layer of REE atoms. A broad composition field for the pyrochlore phase and a narrow field for the monoclinic phase are consistent with the data for the system with Nd as the only present lanthanide [35]. In the phase diagram of the $NdO_{1.5}$–$ZrO_2$–$TiO_2$ system, the pyrochlore field (Fig. 1) extends along the $Nd_2Zr_2O_7$–$Nd_2Ti_2O_7$ line to the composition (mol %) 50 $NdO_{1.5}$, 28.5 $ZrO_2$, 21.5 $TiO_2$, which corresponds to the formula $Nd_{2.0}(Zr_{1.14}Ti_{0.86})O_7$. Harvey et al. [37] report somewhat higher Ti content of the pyrochlore phase, 56 mol % $Nd_2Ti_2O_7$, which corresponds to the formula $Nd_2(Zr_{0.89}Ti_{1.11})O_7$.

In the monoclinic phase, the REE content varies in a narrower range, and the Zr concentration does not exceed 2 wt %. This is consistent with the data for the $La_2O_3$–$ZrO_2$–$TiO_2$ system [31], according to which the Zr concentration in the $La_2Ti_2O_7$ phase does not exceed 1.3 mol % $ZrO_2$. On the whole, the broad stability field is a positive feature of the matrices, because in this case the formation of other phases at deviations of the gross composition from the target values (e.g., owing to variations in the waste composition or to errors in charge preparation) can be avoided. This fact is of particular importance if the additional phases exhibit low resistance in water and thus deteriorate the protective properties of the matrix. However, the phase composition of HLW matrices and their isolation properties can also be influenced by the valence state of actinides and cerium as waste components.

## CERIUM VALENCE IN THE CUBIC AND MONOCLINIC PHASES

The valence of elements in a matrix is influenced by temperature and oxidation conditions (oxygen pressure). The temperature elevation acts in the same direction as a decrease in the oxidation potential. The reduction of variable-valence elements with increasing temperature at a constant partial pressure of oxygen is associated with this fact. For example, $UO_3$ transforms on heating into $U_3O_8$ and $U_4O_9$; $Fe_2O_3$, into $Fe_3O_4$ and FeO; and $CeO_2$, into $Ce_2O_3$.

The shape of the X-ray absorption curves for sample T4 consisting exclusively of the pyrochlore phase (Fig. 4) shows that cerium is present in the tetravalent state as in $CeO_2$. In sample T18 with the prevalent monoclinic phase, the shift of the absorption edge and changes in the shape of the cerium $L_2$ and $L_3$ lines are associated with $Ce^{3+}$, although the weak peak near 5740 eV suggests the presence of a small amount of $Ce^{4+}$. Taking into account the phase composition of these samples, we can conclude that the pyrochlore phase contains $Ce^{4+}$ only, whereas in monoclinic titanate cerium is present as $Ce^{3+}$.

It should be noted that sample T4 was prepared in air at 1550°C, whereas sample T18 was synthesized at a lower temperature, 1400°C. Along with the temperature and oxygen pressure, the valence of the element is influenced by structural features of phases stabilizing definite states of cerium and actinides in them [8, 44–47]. For example, under the conditions of sintering in air, cerium occurs in the form of $Ce^{4+}$ in pyrochlore and zirconolite, the fraction of $Ce^{4+}$ in REE silicate of britolite structure is 90%, whereas in the phosphate (monazite) it is present as $Ce^{3+}$. In zirconolite, the $Pu^{4+}$ contribution decreases from 100% to 0 on replacement of oxidizing (air) or inert (Ar) atmosphere by reducing

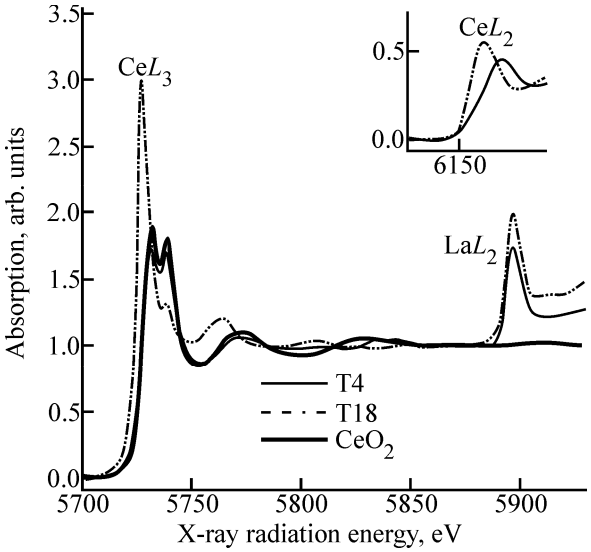


**Fig. 4.** X-ray absorption fine structure of cerium $L_2$ and $L_3$ lines for sample T4 consisting of pyrochlore and sample T18 with the prevalence of the monoclinic phase.

atmosphere ($H_2/N_2$). Cerium behaves similarly to Pu, and for Np oxidation state IV is characteristic even under reducing conditions. The valence of elements in perovskite ($CaTiO_3$) is influenced by the composition [46]; Ce and Pu can occur in it in the trivalent state even when the synthesis is performed in air. The leach rate of actinides and REE in the trivalent state from the matrix with an aqueous solution is higher than that of tetravalent cations, which should be taken into account when choosing actinide phases and conditions of their synthesis.

## ISOLATION PROPERTIES OF CUBIC AND MONOCLINIC PHASES

The stability of an actinide matrix in solutions is characterized by the leach rate of elements from it. Various static and dynamic tests are used for determining the leach rates, in particular, the procedures developed by the Materials Characterization Center in the United States: MCC-1, MCC-2, MCC-3, MCC-4 [1]. The conditions of these tests differ in the weight ratio of the liquid and solid phases, form of the waste matrix (monolithic specimen or powder), and other parameters.

The behavior of pyrochlore matrices in solutions has been studied in much detail (see [1, 3, 10, 11, 14] and other papers). The actinide and REE leach rates at pH in the range from 2 to 12 at 95°C varies from $10^{-4}$ to $10^{-6}$ g $m^{-2}$ $day^{-1}$; higher values are characteristic of titanate matrices, and lower values, of zirconate pyrochlores. The corrosion resistance of monoclinic titanate is less studied. The Ce concentration in a 0.1 M NaCl solution after 60-day contact with a $Ce_2Ti_2O_7$ powder at 25 and 50°C [36] appeared to be below detection limit equal to $2 \times 10^{-4}$ wt %, and in a more aggressive 0.1 M HCl solution it was 0.03 wt %. Taking into account the sample surface area and the time of its interaction with the solution, this corresponds to the Ce leach rate lower than $10^{-5}$ g $m^{-2}$ $day^{-1}$ in a 0.1 M NaCl solution and $10^{-3}$ g $m^{-2}$ $day^{-1}$ in a 0.1 M HCl solution. According to the requirements to properties of HLW matrices, the Pu leach rate should be lower than $10^{-3}$ g $m^{-2}$ $day^{-1}$ [48]. Assuming similar behavior of trivalent Ce and Pu cations, these data allow monoclinic REE titanate to be considered as resistant to leaching. However, this conclusion requires additional experimental check.

With time, the crystal lattice of the phases undergoes changes due to accumulation of defects caused by the actinide decay. This will ultimately lead to disordering of the atoms in the structure (amorphization). This is manifested as disappearance of peaks from the X-ray diffraction patterns and appearance of broad rings in the electron diffraction patterns instead of point reflections. The actinide leach rate from the matrices usually increases after amorphization by less than an order of magnitude, but in some cases it increases by a factor of 20–50 [3, 10, 11].

## RADIATION RESISTANCE OF CUBIC AND MONOCLINIC PHASES

The following approaches are used in studying the radiation resistance of actinide matrices: irradiation with accelerated charged (metal or inert gas cations) and neutral particles (neutrons), synthesis and study of artificial phases containing short-lived isotopes ($^{238}$Pu, $^{241,243}$Am, $^{244}$Cm, $^{249}$Cf), study of their natural analogs (radioactive minerals), and computer modeling. All these methods were applied to studying pyrochlore matrices (see [3, 7, 9–11, 13, 49–54] and other papers). The radiation resistance of a crystalline phase is quantitatively characterized by the critical amorphization dose and critical amorphization temperature. The critical amorphization temperature is the temperature above which the lattice disordering does not occur at any magnitude of the radiation action. If the critical amorphization temperature is in the range of temperature in an underground high-level waste repository

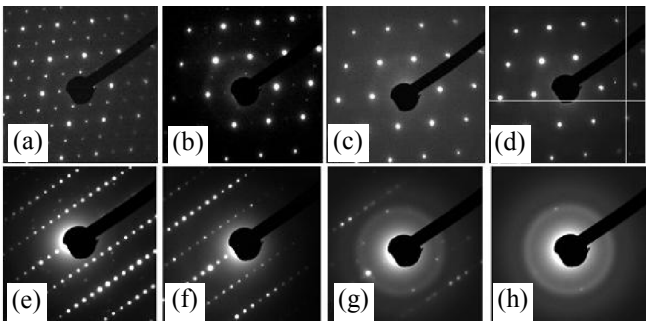


**Fig. 5.** Evolution of the electron diffraction patterns of (a–d) pyrochlore (T0) and (e–h) perovskite (T18) phases in the course of irradiation with 1-MeV $Kr^{2+}$ ions (25°C). (a, e) Initial samples; fluence, $10^{14}$ ions $cm^{-2}$: (b) 2.0, (c) 6.2, (d) 25.0, (f) 1.25, (g) 1.9, and (h) 2.5.

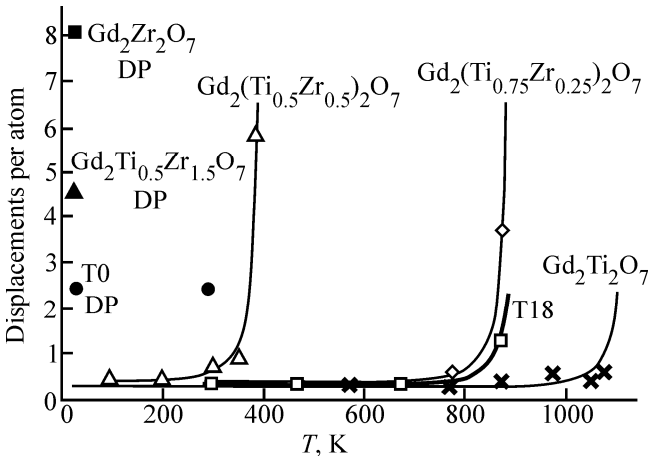


**Fig. 6.** Critical dose in irradiation with 1-MeV $Kr^{2+}$ ions as a function of temperature for pyrochlores of the compositions $Gd_2(Ti_{1-x}Zr_x)_2O_7$ [49], zirconate pyrochlore in sample T0, and monoclinic REE titanate phase in sample T18. The structure of the phases of $Gd_2Zr_2O_7$, $Gd_2(Ti_{0.5}Zr_{1.5})_2O_7$, and zirconate pyrochlore in sample T0 transform in the course of irradiation into a defective fluorite lattice without amorphization.

(25–250°C [11]), the matrix will not undergo amorphization and will preserve its properties.

Irradiation of zirconate pyrochlore (sample T0) with 1-MeV $Kr^{2+}$ ions leads to disappearance of weak reflections from the electron diffraction pattern, and the lattice transforms into a fluorite-type structure, which is preserved at the highest dose, $25 \times 10^{14}$ (Kr ions) $cm^{-2}$ (Fig. 5). After irradiation of monoclinic titanate (T18 and T20) to a considerably lower dose, broad rings appear in the electron diffraction pattern instead of point maxima, suggesting disordering of the structure. The amorphization dose is $3 \times 10^{14}$ ions $cm^{-2}$, which is close to the values for $La_2Ti_2O_7$ of the same structure [38–40] and to the values for titanate pyrochlores, murataite, and ferrite garnet [1, 3]. Various calculation procedures are used for converting the ionic irradiation dose to more universal characteristics (number of displacements per lattice atom) [11, 50]. As shown in our previous studies [3, 50], in irradiation of matrices with 1-MeV $Kr^{2+}$ ions the fluence of $10^{14}$ ions $cm^{-2}$ approximately corresponds to 0.1 displacement per atom.

The higher the critical dose is and the lower the critical temperature is, the more radiation-resistant is the structure of the HLW matrix. REE titanates of perovskite structure undergo amorphization at small doses, whereas zirconate pyrochlores are resistant to radiation even at low temperatures (Fig. 6). At very high irradiation doses and low temperatures, zirconate pyrochlores undergo weak disordering of atoms with transformation of the pyrochlore structure into a fluorite-type lattice. Amorphization of pyrochlore with the Ti/Zr atomic ratio of approximately 1 will occur within several thousands of years [11], and for monoclinic titanate it will occur already within 100 years. The radiation resistance of monoclinic titanate is close to that of the Ti–Zr pyrochlore of the composition $Gd_2(Ti_{1.5}Zr_{0.5})O_7$ (Fig. 6).

## CONCLUSION

Phases of the $REE_2Zr_2O_7$–$REE_2Ti_2O_7$ system are of interest as matrices for immobilization of the rare earth–actinide fraction of waste from spent nuclear fuel reprocessing. The rare-earth elements required for the formation of these phases are already present in the waste, and to prepare the matrices it is necessary to add titanium oxide, zirconium oxide, or their mixture. The structure of the major phases of the matrix is determined by its composition. Up to $x = 0.8$ in the sample formula $REE_2(Zr_{2-x}Ti_x)O_7$, the matrices consist of pyrochlore, and at higher Ti content they contain pyrochlore and monoclinic REE titanate of perovskite structure. The monoclinic phase becomes prevalent at $x > 1.2$. It surpasses zirconate pyrochlore in the capacity for the waste components. Its radiation resistance is close to that of titanate pyrochlore and is lower than that of zirconate and titanate–zirconate pyrochlores. According to published data, this phase is stable in aqueous solutions. To evaluate the suitability of the monoclinic titanate for immobilization of the rare earth–actinide waste fraction, it is necessary to study the effect of the matrix amorphization on the actinide leach rate. The matrix can be prepared using the cold

pressing–sintering method suggested in the United States for immobilization of excess weapons plutonium in pyrochlore matrices. Another procedure is cold crucible induction melting followed by crystallization. We used this procedure previously [5] for preparing a matrix based on titanate–zirconate pyrochlore whose melting point is higher by 300°C than that of the monoclinic titanate of perovskite structure [30].

## ACKNOWLEDGMENTS

The study was performed within the framework of a budget research theme and was supported by the Russian Foundation for Basic Research (project nos. 13-05-00 085 and 14-05-31 034). The authors are grateful to L.A. Kochetkova (Institute of Geology of Ore Deposits, Petrography, Mineralogy, and Geochemistry, Russian Academy of Sciences) for the assistance in performing the X-ray diffraction analysis, to Ya.V. Zubavichus (Kurchatov Institute) for recording the XAFS spectra, and to J. Zhang (Michigan University, the United States) for performing the sample irradiation.

The authors are grateful to the referees of the paper for remarks and valuable recommendations.

## REFERENCES

1. Laverov, N.P., Velichkin, V.I., Omel'yanenko, B.I., et al., *Izolyatsiya otrabotavshikh yadernykh materialov (geologo-geokhimicheskie osnovy)* (Isolation of Spent Nuclear Materials (Geological and Geochemical Principles)), Moscow: Inst. Fiziki Zemli, Ross. Akad. Nauk, 2008.
2. Laverov, N.P., Yudintsev, S.V., Stefanovsky, S.V., and Jang, Y.N., *Dokl. Earth Sci.*, 2001, vol. 381A, no. 9, pp. 1053–1056.
3. Laverov, N.P., Yudintsev, S.V., Livshits, T.S., et al., *Geochem. Int.*, 2010, vol. 48, no. 1, pp. 1–14.
4. Yudintsev, S.V., *Geol. Ore Deposits*, 2003, vol. 45, no. 2, pp. 151–165.
5. Yudintsev, S.V., Stefanovsky, S.V., and Nikonov, V.S., *Dokl. Earth Sci.*, 2014, vol. 454, no. 1, pp. 54–58.
6. Lumpkin, G.R., *Elements*, 2006, vol. 2, no. 6, pp. 365–372.
7. Ewing, R.C., *Earth Planet. Sci. Lett*., 2005, vol. 229, pp. 165–181.
8. Hayatt, N.C., Stennet, M., Jenni, A., et al., *Mater. Res. Soc. Symp. Proc*., 2009, vol. 1193, pp. 61–66.
9. Ewing, R.C. and Weber, W.J., *The Chemistry of the Actinide and Transactinide Elements*, Morss, L.R., Edelstein, N.M., Fuger, J., Eds., Dordrecht (Netherlands): Springer, 2010, vol. 6, ch. 35, pp. 3813–3889.
10. Burakov, B.E., Ojovan, M.I., and Lee, W.E., *Crystalline Materials for Actinide Immobilization. Materials for Engineering*, London: Imperial College Press, 2011, vol. 1.
11. Ewing, R.C., Weber, W.J., and Lian, J., *J. Appl. Phys*., 2004, vol. 95, no. 11, pp. 5949–5971.
12. Ebbinghaus, B.B., Van Konynenburg, R.A., Vance, E.R., et al., US Patent 6 137 025, 1999.
13. Strachan, D.M., Scheele, R.D., Buck, E.C., et al., *J. Nucl. Mater*., 2005, vol. 345, pp. 109–135.
14. Icenhower, J.P., Strachan, D.M., McGrail, B.P., et al., *Am. Mineral*., 2006, vol. 91, pp. 39–53.
15. Ewing, R.C., *Can. Mineral*., 2005, vol. 43, pp. 2099–2116.
16. Myasoedov, B.F., in *Materialy seminara "Mezhdunarodnoe khranilishche obluchennogo yadernogo topliva"* (Proc. Workshop "International Spent Nuclear Fuel Repository"), Moscow, May 14–15, 2003, Moscow: Avangard, 2005, pp. 248–258.
17. *Implications of Partitioning and Transmutation in Radioactive Waste Management*, Vienna: IAEA, 2004.
18. Kopyrin, A.A., Karelin, A.I., and Karelin, V.A., *Tekhnologiya proizvodstva i radiokhimicheskoi pererabotki yadernogo topliva* (Technology for Production and Radiochemical Reprocessing of Nuclear Fuel), Moscow: Atomenergoizdat, 2006.
19. *Treatment and Recycling of Spent Nuclear Fuel*, Paris: CEA, 2008.
20. *National Program in Chemical Partitioning*, Paris: NEA OECD, 2010.
21. Nash, K.L., Madic, Ch., Mathur, J.N., and Lacquement, J., *The Chemistry of the Actinide and Transactinide Elements*, Morss, L.R., Edelstein, N.M., Fuger, J., Eds., Dordrecht (Netherlands): Springer, 2010, vol. 4, ch. 24, pp. 2622–2798.
22. Bruno, J. and Ewing, R.C., *Elements*, 2006, vol. 2, pp. 343–349.
23. Walker, C.T., Rondinella, V.V., Papaioannou, D., et al., *J. Nucl. Mater*., 2005, vol. 345, pp. 192–205.
24. Ivanets, D.V., Tananaev, I.G., and Sarychev, G.A., *Tsvetn. Met.*, 2010, no. 3, pp. 66–72.
25. Collins, E.D., Jubin, R.T., DelCul, G.D., et al., in *Proc. Int. Conf. "Global 2009,"* Paris (France), Sept. 06–11, 2009, pp. 2595–2602.
26. Subramanian, M.A., Aravamudan, G., and Subba Rao, G.V., *Prog. Solid State Chem*., 1983, vol. 15, pp. 55–143.
27. Shoup, S.S. and Bamberger, C.E., *Mater. Res. Soc. Symp. Proc*., 1997, vol. 465, pp. 379–386.
28. Laverov, N.P., Yudintsev, S.V., Stefanovsky, S.V., et al., *Dokl. Earth Sci.*, 2002, vol. 383, no. 2, pp. 190–193.

29. Stefanovsky, S.V., Yudintsev, S.V., and Nikonov, B.S., *Fiz. Khim. Obrab. Mater.*, 2004, no. 2, pp. 68–77.
30. Gong, W. and Zhang, R., *J. Alloys Compd*., 2013, vol. 548, pp. 216–221.
31. Skapin, S.D., Kolar, D., and Suvorov, D., *Solid State Sci*., 1999, vol. 1, pp. 245–255.
32. Skapin, S.D., Kolar, D., and Suvorov, D., *J. Eur. Ceram. Soc*., 2000, vol. 20, pp. 1179–1185.
33. Preuss, A. and Gruehn, R., *J. Solid State Chem*., 1994, vol. 110, pp. 363–369.
34. Gong, W. and Zhang, R., *Thermochim. Acta*, 2012, vol. 534, pp. 28–32.
35. Shoup, S.S., Bamberger, C.E., Tyree, J.L., and Anovitz, L.M., *J. Solid State Chem*., 1996, vol. 127, pp. 231–239.
36. Shoup, S.S., Bamberger, C.E., Haverlock, T.J., and Peterson, J.R., *J. Nucl. Mater*., 1997, vol. 240, pp. 112–117.
37. Harvey, E.J., Whittle, K.R., Lumpkin, G.R., et al., *J. Solid State Chem*., 2005, vol. 178, no. 3, pp. 800–810.
38. Smith, K.L., Blackford, M.G., Lumpkin, G.R., et al., *Microsci. Microanal*., 2006, vol. 12, suppl. 2, pp. 1094–1095.
39. Whittle, K.R., Lumpkin, G.R., Smith, K.L., et al., *Mater. Res. Soc. Symp. Proc*., 2007, vol. 985, CD-version, paper 0985-NN08-09.
40. Whittle, K.R., Lumpkin, G.R., Blackford, M.G., et al., *J. Solid State Chem*., 2010, vol. 183, pp. 2416–2420.
41. Laverov, N.P., Yudintsev, S.V., Stefanovsky, S.V., and Ewing, R.Ch., *Dokl. Earth Sci.*, 2012, vol. 443, no. 2, pp. 526–531.
42. Shannon, R.D., *Acta Crystallogr., Sect. A*, 1976, vol. 32, no. 5, pp. 751–767.
43. *PDFWIN-2*, Int. Centre for Diffraction Data, Newton Square, PA (USA), 1999.
44. Begg, B.D., Vance, E.R., Day, R.A., et al., *Mater. Res. Soc. Symp. Proc*., 1997, vol. 465, pp. 325–332.
45. Begg, B.D. and Vance, E.R., *Mater. Res. Soc. Symp. Proc*., 1997, vol. 465, pp. 333–340.
46. Begg, B.D., Vance, E.R., and Lumpkin, G.R., *Mater. Res. Soc. Symp. Proc*., 1998, vol. 506, pp. 79–86.
47. Fortner, J.A., Kropf, A.J., Bakel, A.J., et al., *Mater. Res. Soc. Symp. Proc*., 2000, vol. 608, pp. 401–406.
48. *GOST* (State Standard) *R 50926–96: Solidified High-Level Waste. General Technical Requirements*, Moscow: Izd. Standartov, 1996.
49. Wang, S.X., Begg, B.D., Wang, L.M., et al., *J. Mater. Res*., 1999, vol. 14, no. 12, pp. 4470–4473.
50. Laverov, N.P., Yudintsev, S.V., Yudintseva, T.S., et al., *Geol. Ore Deposits*, 2003, vol. 45, no. 6, pp. 423–451.
51. Sykora, R.E., Raison, P.E., and Haire, R.G., *J. Solid State Chem*., 2005, vol. 178, pp. 578–583.
52. Lumpkin, G.R., Pruneda, M., Rios, S., et al., *J. Solid State Chem*., 2007, vol. 180, pp. 1512–1518.
53. Laverov, N.P., Yudintsev, S.V., Velichkin, V.I., et al., *Radiochemistry*, 2009, vol. 51, no. 5, pp. 529–536.
54. Stefanovsky, S.V., Yudintsev, S.V., and Myasoedov, B.F., *Dokl. Chem.*, 2012, vol. 447, no. 2, pp. 296–299.

*Translated by G. Sidorenko*